

# Preparation and stability of the hexagonal phase of samarium oxide on Ru (0001)

Emilia Pożarowska<sup>a</sup>, Linus Pleines<sup>b</sup>, Moritz Ewert<sup>a</sup>, Mauricio J. Prieto<sup>c</sup>, Liviu C. Tănase<sup>c</sup>, Lucas de Souza Caldas<sup>c</sup>, Aarti Tiwari<sup>c</sup>, Thomas Schmidt<sup>c</sup>, Jens Falta<sup>b</sup>, Eugene Krasovskii<sup>d,e,f</sup>, Carlos Morales<sup>a</sup>, Jan Ingo Flege<sup>a,\*</sup>

<sup>a</sup> Applied Physics and Semiconductor Spectroscopy, Brandenburg University of Technology Cottbus-Senftenberg, 03046 Cottbus, Germany

<sup>b</sup> Institute of Solid State Physics, University of Bremen, 28359 Bremen, Germany

<sup>c</sup> Department of Interface Science, Fritz-Haber Institute, 14195 Berlin, Germany

<sup>d</sup> Departamento de Polímeros y Materiales Avanzados: Física, Química y Tecnología, Universidad del País Vasco UPV/EHU, 20080 San Sebastián/Donostia, Spain

<sup>e</sup> IKERBASQUE, Basque Foundation for Science, E-48013 Bilbao, Spain

<sup>f</sup> Donostia International Physics Center (DIPC), E-20018 San Sebastián, Spain

## ARTICLE INFO

### Keywords:

Sm<sub>2</sub>O<sub>3</sub>  
LEEM  
XPEEM  
Facets  
Epitaxy  
Hexagonal phase

## ABSTRACT

We have used low-energy electron microscopy (LEEM), micro-illumination low-energy electron diffraction ( $\mu$ LEED) supported by *ab initio* calculations, and X-ray absorption spectroscopy (XAS) to investigate *in-situ* and in real-time the structural properties of Sm<sub>2</sub>O<sub>3</sub> deposits grown on Ru(0001), a rare-earth metal oxide model catalyst. Our results show that samarium oxide grows in a hexagonal A-Sm<sub>2</sub>O<sub>3</sub> phase on Ru(0001), exhibiting a (0001) oriented-top facet and (113) side facets. Upon annealing, a structural transition from the hexagonal to cubic phase occurs, in which the Sm cations exhibit the +3 oxidation state. The unexpected initial growth in the A-Sm<sub>2</sub>O<sub>3</sub> hexagonal phase and its gradual transition to a mixture with cubic C-Sm<sub>2</sub>O<sub>3</sub> showcases the complexity of the system and the critical role of the substrate in the stabilization of the hexagonal phase, which was previously reported only at high pressures and temperatures for bulk samaria. Besides, these results highlight the potential interactions that Sm could have with other catalytic compounds with respect to the here gathered insights on the preparation conditions and the specific compounds with which it interacts.

## 1. Introduction

The tendency for a rare-earth metal oxide (REO) to promote partial or complete oxidation in catalysis depends mainly on the ability of the cation to access higher oxidation states. While all the lanthanides can form stable sesquioxides (Ln<sub>2</sub>O<sub>3</sub>), only a few, such as Ce, Pr, and Tb, can form bulk dioxides and a wide range of intermediate oxide stoichiometries [1]. Nevertheless, rare-earth elements and their oxides are used not only as active catalytic phases but also as structural and electronic promoters to improve the catalysts' activity, selectivity, and thermal stability [2–5]. Therefore, there is a possibility of enhancing the catalytic activity by incorporating promoters through alloying with trivalent catalytically active rare-earth metals that also form cubic sesquioxides (RE<sub>2</sub>O<sub>3</sub>). For example, in the well-known model CeO<sub>x</sub>/Cu system, these dopants could promote the stabilization of the Ce<sup>3+</sup> active sites [6,7] and desired structural phases. Whereas Niu et al. [8] have shown that in

the ternary praseodymium and cerium oxide system increasing the doping of Pr<sup>3+</sup> leads to stabilizing the Ce<sup>3+</sup> valence state. With this insight, Sm has recently attracted attention as a promising candidate to be added as a promoter to the catalysts for different heterogeneous catalytic processes to enhance activity and tune selectivity [9–11]. For instance, Sm<sub>2</sub>O<sub>3</sub>-supported palladium and Sm<sub>2</sub>O<sub>3</sub>-doped CeO<sub>2</sub>/Al<sub>2</sub>O<sub>3</sub>-supported copper have been used as catalysts for CO oxidation [12] and intermediate-temperature methanol fuel cells [13], respectively. However, to optimize the use of Sm in complex REO/metal systems, a deeper understanding of Sm<sub>2</sub>O<sub>3</sub> and its complex interaction with metallic substrates and catalytic REOs is needed.

The study of Sm compounds on different model substrates has traditionally been limited to addressing its mixed valency through spectroscopic techniques, as slight differences in the physicochemical environments around the Sm cations can lead to an exchange between its two nearly degenerate electronic configurations, Sm divalent ([Xe]

\* Corresponding author.

E-mail address: [flege@b-tu.de](mailto:flege@b-tu.de) (J.I. Flege).

<https://doi.org/10.1016/j.ultramic.2023.113755>

Received 22 January 2023; Received in revised form 15 April 2023; Accepted 8 May 2023

Available online 9 May 2023

0304-3991/© 2023 The Author(s). Published by Elsevier B.V. This is an open access article under the CC BY license (<http://creativecommons.org/licenses/by/4.0/>).

$4f^6 (6s5d)^2$ ) and trivalent ( $[Xe]4f^5 (6s5d)^3$ ), and related cations [11, 14–18]. Moreover, polymorphism of  $Sm_2O_3$  has been treated extensively, focusing on possible phase transitions between cubic C- $Sm_2O_3$ , monoclinic B- $Sm_2O_3$ , and hexagonal A- $Sm_2O_3$  polytypes as a function of temperature and pressure [19,20]. In particular, the cubic and monoclinic phases are stable at standard conditions, whereas the A- $Sm_2O_3$  phase has been reported to exist at high temperatures ( $> 2000$  K) [21, 22] and pressures ( $> 2$  bar) [19,23,24]. As these structural studies focused on commercial samaria powders or single crystals [25], potential effects of heteroepitaxial growth and resulting interfacial contributions to the total free energy of the system are not included, which may lead to the stabilization of exotic phases at unusual conditions. Only few studies have focused on the structural characteristics of  $Sm_2O_3$  growth on well-defined surfaces [18,26,27]; for example, the growth on Pt(111) shows significant film/substrate interaction that forces ultrathin samaria to adopt a defective fluorite structure instead of the typical, bulk cubic C- $Sm_2O_3$  [15]. The lack of combined spectroscopic and structural studies on model systems results in a gap in understanding the influence of samaria structure on its chemical behavior. As LEEM/PEEM studies [28,29] have shown for  $CeO_2(100)$  and  $CeO_2(111)$  systems [30,31], there is a close relationship between reactivity and structure in real-time measurements; therefore, acquiring a fundamental understanding of REO catalyst structure is critical to predicting the reactivity and reducibility of these materials, and it is essential to better understand complex systems such as  $SmO_x-CeO_x$ .

In the present study, we provide a coherent overview of the  $Sm_2O_3$ -Ru(0001) system through low-energy electron microscopy (LEEM) and micro-diffraction ( $\mu$ -LEED), photoemission electron microscopy (PEEM), and X-ray absorption spectroscopy (XAS). We will show that  $Sm_2O_3$  grows epitaxially in the hexagonal A- $Sm_2O_3$  phase at mild temperatures (690 K) and high vacuum conditions ( $< 10^{-7}$  mbar), gradually transitioning to the cubic phase when kept at lower temperatures. This initial growth in the A- $Sm_2O_3$  hexagonal arrangement and the variety of different structural phases highlights the complexity of the samaria system and the different potential interactions that Sm could have with other catalytic compounds depending on the preparation conditions and the specific compounds with which it interacts (i.e., the host material and/or substrate).

## 2. Experimental and computational methodology

A polished Ru(0001) single crystal (Mateck) with a nominal orientation better than  $0.1^\circ$  is used as the model-system substrate in this study. The crystal was initially cleaned in situ by successive cycles of sputtering with  $Ar^+$  ions ( $10^{-5}$  mbar) and annealing at 900 K in an oxygen atmosphere ( $pO_2 = 5 \cdot 10^{-7}$  mbar) until clean and flat surfaces were obtained, as confirmed by LEEM,  $\mu$ -LEED, and XAS. After samaria deposition, the Ru(0001) surface cleaning consisted of repeated cycles of surface oxidation with an oxygen cracker at a pressure of  $5 \cdot 10^{-7}$  mbar and subsequent annealing at 1400°C.

The clean Ru(0001) single crystal was then exposed to a molecular oxygen atmosphere at a pressure of  $5 \cdot 10^{-7}$  mbar and a temperature of 690 K. Under these conditions, a  $(2 \times 1)$ -reconstructed oxygen adlayer is formed on the substrate Ru(0001) substrate with an oxygen coverage of around 0.5ML, which in LEEM is readily identified by its characteristic energy-dependent electron reflectivity, the so-called intensity-voltage (I (V)) curve [32]. Subsequently, the samarium oxide was grown under the same conditions (Ru(0001) substrate at 690 K) by thermal reactive evaporation of metallic Sm under the same reactive oxygen atmosphere ( $5 \cdot 10^{-7}$  mbar) using a commercial electron beam evaporator (Focus EFM 3), with a molybdenum crucible loaded with a metallic Sm rod (Alfa Aesar, 99.9%). After samaria evaporation, the sample was cooled down to 350 K at the same  $O_2$  background pressure. Based on the calibration of the evaporator, we estimated that the average growth rate employed in our experiments was 0.15 ML/min.

The LEEM,  $\mu$ -LEED, and XAS-PEEM measurements were carried out

in the SMART spectro-microscope operating at the UE49-PGM undulator beamline at BESSY II synchrotron radiation facility at the Helmholtz Center Berlin (HZB). The aberration-corrected and energy-filtered LEEM/PEEM instrument combines microscopy, diffraction, and spectroscopy techniques, achieving an energy resolution of 180 meV in XPEEM mode and a lateral resolution of 2.6 nm in LEEM mode [33]. In situ  $\mu$ -LEED images were recorded from illuminated areas of 1.5  $\mu$ m in diameter in an electron energy range from 10 eV up to 100 eV. XAS spectra were measured by collecting the secondary electrons while the photon energy was scanned through the range of about 124 to 134 eV and 1067 to 1115 eV across the Sm  $N_{4,5}$  and Sm  $M_{4,5}$  absorption edges, respectively.

Theoretical LEED-I(V) spectra for cubic bixbyite-like and hexagonal  $Sm_2O_3$  crystals [34] were calculated with the *ab initio* Bloch-waves based scattering method, see Ref. [35]. A detailed description of the methodology and its application to rare-earth sesquioxides has been presented in Refs. [36] and [37]. Here, we briefly recap the main aspects of the calculation. The Schrödinger equation is solved for a semi-infinite crystal: the 3D-periodic bulk potential is modified in the surface region, where it smoothly grows to reach the vacuum level. The potential is obtained in the local density approximation of the density functional theory. It includes the singularities at the nuclei, so the calculations are performed in the augmented-plane-wave representation [35]. The inelastic scattering is included by an energy dependent imaginary potential  $-iV_i$ , which is spatially constant in the crystal and vanishes in the vacuum half-space.

## 3. Results and discussion

### 3.1. Growth of hexagonal A- $Sm_2O_3$ phase at mild conditions

This section discusses the growth of samarium oxide on Ru(0001) at mild temperatures ( $\sim 690$  K) with a particular focus on sample morphology and structure. Low-energy electron microscopy (LEEM) and diffraction ( $\mu$ LEED) were used to probe the sample preparation in situ and in real-time and to determine the geometric structure of the samaria deposit.

Figs. 1 and 2 show the sequence of LEEM images and  $\mu$ -LEED patterns recorded during the growth of samaria at an  $O_2$  background pressure of  $5 \cdot 10^{-7}$  mbar and with the Ru(0001) crystal held at a temperature of 690 K. Fig. 1a corresponds to the clean Ru(0001) substrate, showing only atomic steps (thin dark lines) with atomically flat terraces in-between. The corresponding  $\mu$ -LEED pattern (Fig. 2a) exhibits very sharp and intense diffraction spots assigned to first-order Bragg reflections of the Ru(0001) surface, thus confirming a clean surface with no contamination. Once  $O_2$  is introduced, the  $\mu$ LEED pattern in Fig. 2b also shows the well-known  $(2 \times 1)$  periodicity corresponding to the chemisorbed adlayer phase of oxygen on Ru(0001), with 0.5 ML local O coverage confirmed by the I(V) curves [38] (also see Fig. 5). Fig. 1b to f show the early stages of samaria growth at different coverages, demonstrating how it first decorates the step edges of Ru until small, dark points are visible on the terraces. For relatively thick deposits (Fig. 1f and corresponding magnified region in Fig. 1g), the samaria presents a granular morphology, with bright structures between 10 and 15 nm wide and arranged along the direction of the Ru steps. Finally, using a larger field of view, Fig. 1h clearly showcases the preferential accumulation of bright structures along the steps and step bunches of the substrate. We note that the different contrast observed in panels a-c ( $E_{kin} = 12$  eV) and d-h ( $E_{kin} = 17$  eV) is due to different kinetic energies applied during image acquisition.

From a structural point of view, at coverages around  $\sim 0.5$  ML the bright Ru spots are still visible, and  $\mu$ -LEED additionally shows a hexagonal  $(1.38 \times 1.38)$  superstructure in registry with the Ru(0001) substrate (green-solid marks in Fig. 2c), which is indicative of samaria formation as discussed below. As the samaria coverage increases up to 30 ML, these spots become more intense while those related to the

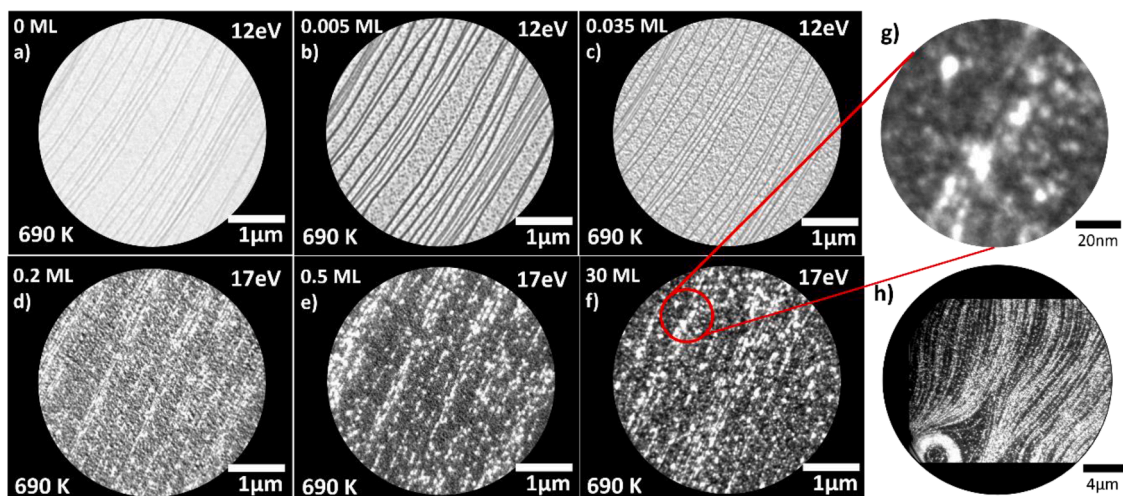


**Fig. 1.** LEEM (FoV = 4  $\mu\text{m}$ ) images of **a)** clean Ru(0001); **(b-f)** time series with different samaria coverages, taken at  $E_{\text{kin}} = 12$  eV (a-c) and  $E_{\text{kin}} = 17$  eV (d-f). **g)** magnified part of LEEM image presented in **f)** showing single islands. **h)** Overview LEEM (FoV = 12  $\mu\text{m}$ ) image illustrating deposition along the step bunches.

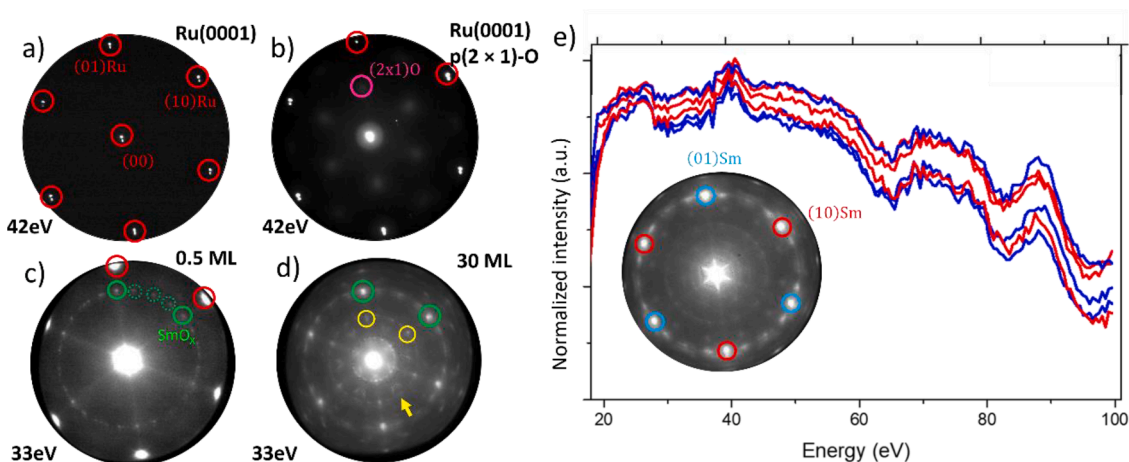


**Fig. 2.**  $\mu$ -LEED patterns obtained during the samaria deposition with  $\mu$ -spot of 1.5  $\mu\text{m}$  **a)** clean Ru(0001) under ultra-high-vacuum conditions at 690 K, **b)** Ru(0001) ( $2 \times 1$ )-O after exposure to  $5 \cdot 10^{-7}$  mbar of  $\text{O}_2$ ; **c)** 0.5 ML of  $\text{Sm}_2\text{O}_3$  showing a hexagonal ( $1.38 \times 1.38$ ) superstructure in azimuthal registry with the Ru(0001) ( $1 \times 1$ ) spots (green solid circles) and some rotated spots, which represent certain rotational domains of the samaria islands (dashed green circles) **d)** 30 ML of  $\text{Sm}_2\text{O}_3$  showing additional  $n/3$  order spots (yellow circle), forming the circular ring (yellow arrow). (a,b) and (c,d)  $\mu$ -LEED patterns taken with  $E = 42$  eV and  $E = 33$  eV, respectively. **e)** Z-axis cut profile through diffraction spot over energy and inserted LEED image taken at the energy of 25 eV. Please note that the apparent “doubling” of the diffraction spots (best visible in **a)**) is an artifact of the Schottky field emitter of the electron gun.

substrate are attenuated. Additionally, between the green-solid-marked  $\text{Sm}_2\text{O}_3$  spots, we observe a faint concentric pattern around the (00) spot, marked with dashed green circles in Fig. 2c. Its appearance suggests the presence of rotational domains of the  $\text{Sm}_2\text{O}_3$  islands, i.e., representing the different possible configurations of how samaria can form a coincidence lattice with the underlying ruthenium surface. For example, an analogous situation was presented by Luches et al. in the ceria/Pt(111) system [39], where several lattice rotations yield a more or less good coincidence between cerium oxide and platinum.

There are two different possibilities to explain the epitaxial growth of samaria forming a hexagonal ( $1.38 \times 1.38$ ) pattern in registry with Ru (0001): cubic C- $\text{Sm}_2\text{O}_3$  (111) or hexagonal A- $\text{Sm}_2\text{O}_3$  (0001). Considering the Ru(0001) integer reflections as a reference, the calculated lattice parameters are  $a_c = 10.56$   $\text{\AA}$  and  $a_A = 3.74$   $\text{\AA}$  for cubic C- $\text{Sm}_2\text{O}_3$  (111) and hexagonal A- $\text{Sm}_2\text{O}_3$  (0001), respectively, whereas in both cases, the Sm-Sm distance is equal to 3.74  $\text{\AA}$ . All these values are in good agreement with the distances reported previously [15,24]. To try to distinguish between cubic C- $\text{Sm}_2\text{O}_3$  (111) and hexagonal A- $\text{Sm}_2\text{O}_3$  (0001), however, qualitative intensity-voltage (I(V)) LEED analysis was employed (Fig. 2e), in which we could check the presence of 3- or 6-fold

symmetry and confirm the existence of either cubic or hexagonal arrangement, respectively. Basically, this method relies on the interpretation that if mirror domains exist, i.e., azimuthal lattice rotations by  $180^\circ$  for cubic  $\text{Sm}_2\text{O}_3$ , then the (01) and (10) symmetrically inequivalent spots should present different I(V) LEED curves for cubic islands with different orientation, whereas hexagonal islands would lead to the same intensities for all spots. The results show that all spots corresponding to samaria (marked as green in Fig. 2) exhibit the same intensities through all sampled electron energies from 10 to 100 eV (see Fig. 2e), thereby suggesting that  $\text{Sm}_2\text{O}_3$ (0001) potentially adopts a hexagonal crystal structure on Ru(0001). However, this result does not yet fully confirm the presence of the hexagonal phase due to the small size of the  $\text{Sm}_2\text{O}_3$  structures (Fig. 1) and the relatively large field of view used in LEEM and the large illuminated area in the LEED measurements: A large number of mirror domains would also yield the same averaged I(V) curves for symmetrically inequivalent spots. Moreover, at the coverage of 30 ML of  $\text{Sm}_2\text{O}_3$ , apart from the intense  $\text{Sm}_2\text{O}_3$ (0001) pattern, additional fractional order spots are observed (marked in yellow in Fig. 2d). These superstructure reflections can be the result of local ordering of the oxygen vacancies, which appear after the extensive growth of the samaria

film. They have a periodicity of  $n/3$  with respect to the first-order samaria spot position. A similar effect was observed in the study of the ceria/Ru system and its reduction by hydrogen [40].

In LEEM instruments, the diffraction spots from flat surfaces do not move in the LEED patterns when changing the energy due to the constant final kinetic energy in the imaging column. Examples with two different energies are displayed in Fig. 3a and 3b. By comparing these two images one can see that some diffraction spots, marked in yellow, move with changing energy. In LEEM systems, this behavior is a clear sign of inclined surface areas, in our case most probably side facets [29]. In order to extract more morphological information, we have performed a detailed analysis of the reciprocal-space map in the  $\text{Sm}_2\text{O}_3$   $[00\bar{1}]-[1\bar{1}0]$  plane, composed of a series of  $\mu$ -LEED patterns taken as a function of electron energy [41,42] from 10 to 100 eV. Fig. 3c shows a cut through this reciprocal-space map from the  $(-10)$  to the  $(10)$  diffraction spot of Ru(0001), setting these Ru spots at a distance of  $(2\pi/2.35) \text{ \AA}^{-1}$  from (00) as calibration. The most intense reciprocal-lattice rods (solid green lines) with a spacing of  $(2\pi/3.24) \text{ \AA}^{-1}$  are attributed to integer reciprocal-lattice rods of the  $\text{Sm}_2\text{O}_3(0001)$  surface. Marked with dashed purple lines, we observe a second pair of less intense vertical rods corresponding to the  $n/3$  order of  $\text{Sm}_2\text{O}_3(0001)$ . The orientation of the abovementioned side facets can be determined from the inclination angles of the related reciprocal-lattice rods, while their absolute spacing correlates with the in-plane lattice. In our case, tilted reciprocal-space rods (light-brown dashed lines) show a spacing of  $(2\pi/16.3) \text{ \AA}^{-1}$  and an angle of  $48^\circ$  (relative to the  $\text{Sm}_2\text{O}_3(0001)$  direction). Therefore, they can be attributed to the presence of  $\text{Sm}_2\text{O}_3(11\bar{3})$  facets in the hexagonal structure, with an expected real-space periodicity of  $16.5 \text{ \AA}$  and inclination angle of  $46.5^\circ$ , in excellent agreement with the experiment. Additionally, the intersection between non-vertical lattice rods and the fundamental rods of a flat surface at bulk Bragg peak conditions reflects the spacing between  $\text{Sm}_2\text{O}_3(0001)$  planes [43]. The value of  $12.1 \text{ \AA}$ , obtained from the vertical distance of this intersection, agrees with the expected value of  $12.02 \text{ \AA}$ .

The previous analysis strongly supports the conclusion of  $\text{Sm}_2\text{O}_3$  growing in the hexagonal A- $\text{Sm}_2\text{O}_3$  phase on Ru(0001) at mild conditions, which contrasts with previous reports using bulk powder samples that only show stabilization of the hexagonal phase at high pressures and temperatures. Indeed, the mild conditions used in this work ( $\sim 10^{-7}$  mbar and 690 K) highlight the critical role of the  $\text{Sm}_2\text{O}_3/\text{Ru}(0001)$  interaction in the stabilization of this exotic structural phase.

Low-energy electron microscopy (LEEM) also allows to measure changes in the work function of samples surfaces by scanning the start voltage  $V_0$  applied to the sample and determining the transition between mirror electron microscopy (MEM) mode, where all electrons are

reflected before reaching the surface, and the LEEM mode, where they interact with the sample. The transition between MEM and LEEM is accompanied by a steep drop in the intensity of reflected electrons in the I-V curve (intensity vs start voltage  $V_0$ ), which depends on the surface potential and the work function (WF) [32,44,45]. During the deposition of  $\text{Sm}_2\text{O}_3$  on Ru(0001), relative changes in the WF are observed (see Fig. 4). Initial oxygen adsorption on the clean substrate surface increases the work function to about 6.3 eV for 0.5 ML O coverage [46], subsequently decreasing after samaria deposition as a function of the total coverage. After the deposition of the first 0.5 ML, a drastic change of 1.4 eV in WF could be identified. As the growth process is continued this shift saturates, resulting in a WF of about 4.3 eV for  $\text{Sm}_2\text{O}_3$ . Similar behavior was already observed after samarium deposition on different substrates, such as Mo [16], Si [47], and  $\text{Al}_2\text{O}_3$  [18].

### 3.2. Stability of hexagonal phase: transition from A- $\text{Sm}_2\text{O}_3$ to C- $\text{Sm}_2\text{O}_3$

In order to check the stability of the A- $\text{Sm}_2\text{O}_3$  phase, the sample was kept at an  $\text{O}_2$  background pressure of  $5 \cdot 10^{-7}$  mbar and cooled down to 350 K, preventing any further contamination of the sample surface. Fig. 5 shows a time-dependent sequence of I(V) curves that have been

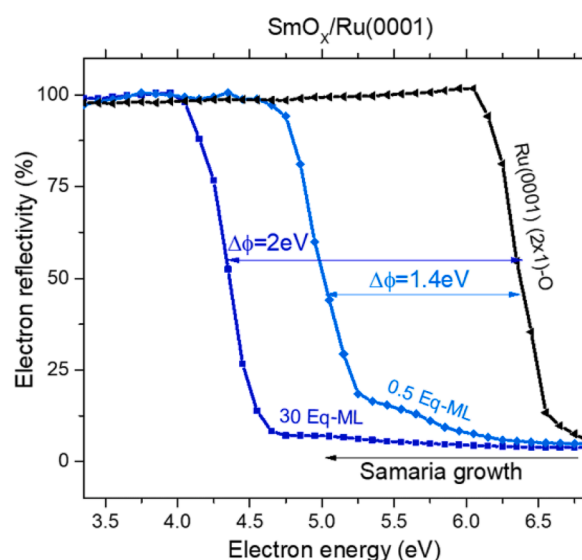


Fig. 4. I(V) curves zoom on the transition between MEM and LEEM modes. Black curve: Ru(0001)  $(2 \times 1)$ -O, light-blue curve: 0.5 Eq-ML of samaria, dark-blue curve: 30 Eq-ML of samaria.

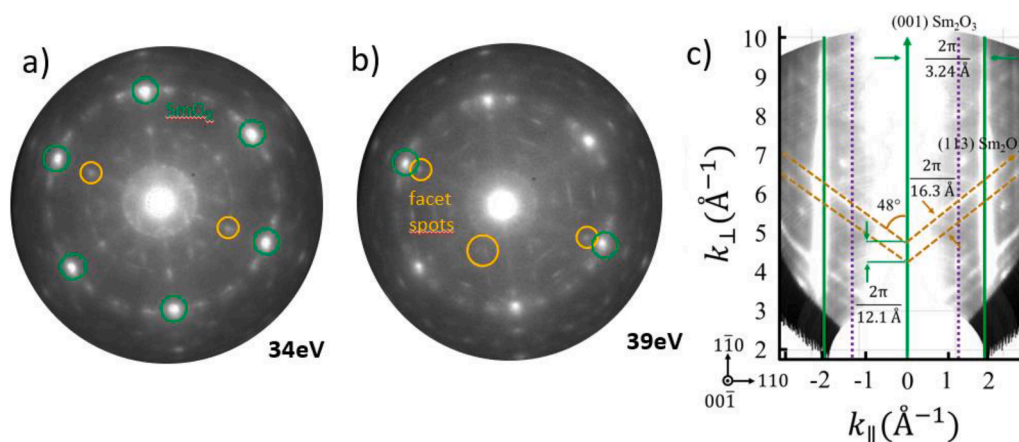
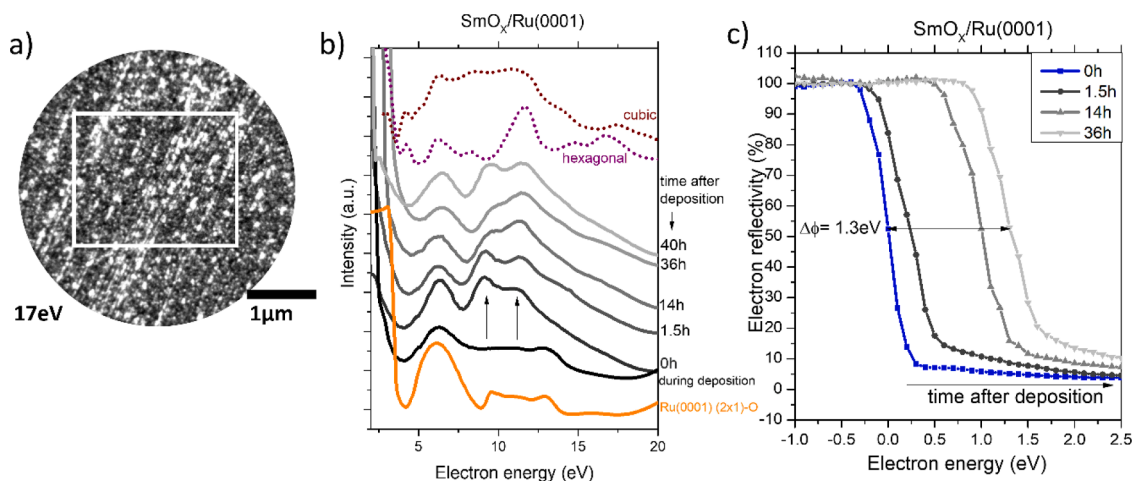


Fig. 3. a) and b)  $\mu$ LEED patterns acquired of the  $\text{Sm}_2\text{O}_3/\text{Ru}(0001)$  surface. c) Reciprocal-space map in the  $\text{Sm}_2\text{O}_3$   $[00\bar{1}]-[1\bar{1}0]$  plane, revealing the side facet orientations and inclination of the samaria islands.



**Fig. 5.** (a) Respective sample area investigated in measurements of (b). (b) Evolution of I(V) spectra of  $\text{Sm}_2\text{O}_3/\text{Ru}(0001)$  with the time while keeping the sample 350 K (black/gray). Comparison with the calculations of cubic and hexagonal phases (brown and purple). Orange: Ruthenium substrate with chemisorbed oxygen adlayer ( $2 \times 1$ )-O. I(V) curves taken from the area as indicated by the white rectangle in the LEEM image (a). (c) Changes in the work function with the time after the end of the deposition, sample kept at 350 K.

recorded up to 40 h after the end of the evaporation. In detail, the I(V)-LEEM analysis offers a fingerprint to identify the local atomic structure by comparing the experimental curves with those obtained from reference structures, thus providing a local dynamic evolution study of the sample morphology [32]. The bottom, orange I(V) curve is assigned to clean Ru(0001) with 0.5 ML of chemisorbed oxygen, which, as previously shown, is formed after initial exposure to  $\text{O}_2$  [38] and before  $\text{Sm}_2\text{O}_3$  deposition. The black lines show the evolution of the  $\text{Sm}_2\text{O}_3/\text{Ru}$  I(V) curves, starting from measurements during deposition and finishing 40 h after the evaporation was completed. The first measurements labeled 0 h and 1.5 h, i.e. taken just after the deposition and 1.5 h later, respectively, show robust bumps at electron energies around 6 and 9 eV. Gradually, a moderate decrease of those features is observed, while at the same time, at 12 eV the reflectivity increases. After 40 h, these three bumps show a similar intensity, decreasing the relative depth of the valley at around 7.5 eV.

To achieve a more detailed interpretation, we have compared the experimental data with the theoretical reflectivity curves calculated using *ab initio* scattering theory from crystalline surfaces as summarized in the methodology section. The calculations have been performed for the cubic C- $\text{Sm}_2\text{O}_3$  and hexagonal A- $\text{Sm}_2\text{O}_3$  systems (top brown and purple curves in Fig. 5b, respectively). We observe that an intense feature at 12 eV characterizes the hexagonal phase, while the cubic structure shows a broader bump composed of three maxima at 6, 9, and 12 eV. At the early stages of growth, the noticeable features at 6 and 9 eV could be related to metallic samarium that fully oxidizes with time. Furthermore, by directly comparing the experimental and theoretical curves, we can interpret the changes from  $t = 14$  h in a gradual transition from the hexagonal to cubic phase. We should note here that the previously described analysis of the data presented in Figs. 2 and 3 showing the hexagonal arrangement of  $\text{Sm}_2\text{O}_3$  was done using  $\mu$ -LEED patterns measured 14 h after deposition, precisely when the characteristic bump at 12 eV of the hexagonal phase is more pronounced. Moreover, after 40 h, the experimental I(V) curve resembles the I(V) curve calculated for the cubic phase, indicating a gradual structural change. Finally, as has been extensively discussed already [48–50], the work function, surface energy, and crystal orientation are strongly correlated. The continuous relative change of the WF by 1.3 eV after 36 h shown in Fig. 5c supports the notion that a structural change occurs in the samaria film after stopping the evaporation.

To confirm the transition from hexagonal to cubic phase (probably not completely, but rather into a mixture dominated by the cubic structure), we have performed dark-field (DF) imaging. In this mode, a

non-specular diffraction beam is used for creating the real-space image, so only the surface regions contributing to the overall intensity of the selected LEED spots will appear bright, establishing a direct correlation between real and reciprocal space features. The DF measurements presented in Fig. 6 were performed between 36 and 40 h after the end of the deposition, at the time when the transition between hexagonal and cubic phases was mostly finished (as shown by I(V) curves in Fig. 5b). In order to check the correlation between real and reciprocal space, we adopted the following procedure: First, the reference bright-field (BF) image was collected (Fig. 6b), where all sample regions appearing bright significantly contribute to the high (00) beam intensity at this given electron

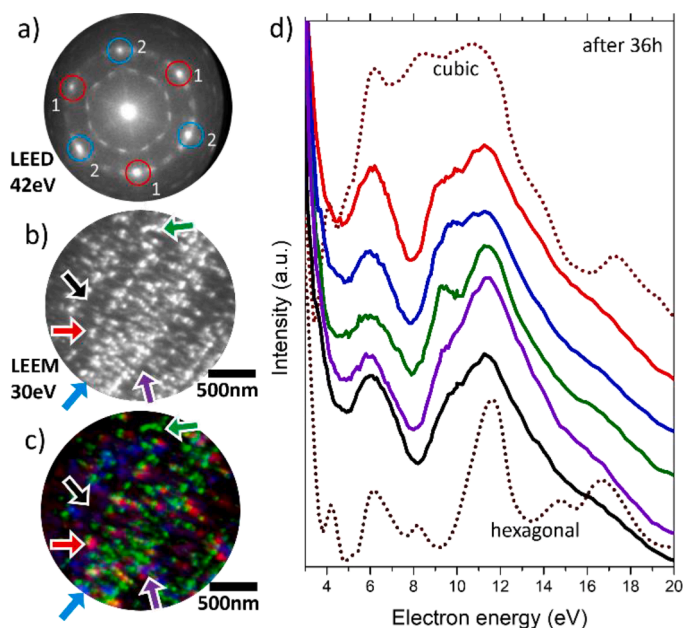


**Fig. 6.** a) Low-energy electron diffraction pattern acquired after samarium oxide growth ( $E = 42$  eV). The reflections of  $\text{Sm}_2\text{O}_3$  are labeled. b) Bright-field (BF) LEEM image and c) composite image consisting of BF image (in (b)) and two DF-LEEM images recorded using  $\text{Sm}_2\text{O}_3$  reflections marked as (1) (red-false color) and (2) (blue-false color). All those features of the BF image that do not coincide with marked samaria islands in the DF images are shown in green-false color in (c). d) I(V) curve of  $\text{Sm}_2\text{O}_3$  marked with arrows in (b-c), taken 36 h after deposition, compared with calculated curves from hexagonal and cubic phases.

energy. Next, a false-color DF image is created using first-order reflections of the samaria lattice (marked in red and blue in Fig. 6a), highlighting the possible orientation of the features and the 3-fold and 6-fold symmetry associated with the cubic and hexagonal phases, respectively.

In more detail, DF images of cubic  $\text{Sm}_2\text{O}_3$  are only expected to be derived from LEED spots taken in three-fold symmetry arrangement, i.e. either red (1) or blue (2) circles. Indeed, the false-color composite image in Fig. 6c shows some features colored in red and blue exclusively associated with those diffraction spots, respectively, confirming the existence of a three-fold symmetry consistent with the cubic structure. Furthermore, some features are bright in all DF images, overlapping in the composite image (purple color). This behavior points to the six-fold symmetry and suggests that some particles have retained their hexagonal phase. The previous observations are confirmed in Fig. 6cc and d by local I(V) curves taken from individual islands (see arrows in Fig. 6d and c; curves, arrows and islands share the same colors). Red and blue islands present I(V) curves similar to the calculated cubic phase curve, whereas those curves taken from the purple islands present a more pronounced bump at 12 eV while the intensity at 6 and 9 eV decreases, which based on our calculations is characteristic of the hexagonal phase. Intriguingly, the composite of all DF images cannot reproduce the bright-field image: all regions that appear bright in the BF image and do not appear in any DF image, i.e., they do not contribute to the main samaria LEED spots, are colored in green in Fig. 6c. Although the I(V) curve from these regions resembles the theoretical one from the cubic phase, it also presents a slightly different shape, suggesting that these are  $\text{Sm}_2\text{O}_3$  islands grown with different orientations on the Ru(0001) substrate and which exhibit small structural differences, e.g., a slight variation in oxygen content. This finding is in contrast to the results of an analogous LEEM/XPEEM study of the related system  $\text{CeO}_2(111)/\text{Ru}(0001)$ , where azimuthal rotations of the ceria islands were not correlated with any noticeable differences in the respective I(V) curves [38].

Finally, local XAS-PEEM measurements were performed to determine the oxidation state of samaria and check for possible variations in the near edge X-ray absorption fine structure spectra (NEXAFS). The latter technique is also sensitive to the local atomic environment because of variations in the crystal field symmetry or ligand-cation hybridization [51]. Fig. 7a displays the LEEM image taken with FoV of 2  $\mu\text{m}$  where the local XAS spectra were measured, distinguishing between bright (blue spectra) and dark (red spectra) regions. The photon energy was tuned through the  $\text{Sm } M_{4,5}$  and  $\text{Sm } N_{4,5}$  edges, as shown in Fig. 7a and b, respectively. On the one hand, the  $\text{Sm } M_{4,5}$  edge spectra indicate that samaria is fully oxidized to  $\text{Sm}^{3+}$  [52,53] ( $\text{Sm}_2\text{O}_3$ ) on every part of the sample, without traces of  $\text{Sm}^{2+}$  [54,55] or metallic Sm. This result discards possibly significantly different degrees of oxidation that could influence the I(V) curves, highlighting the structural origin of those changes. On the other hand,  $\text{Sm } N_{4,5}$ -edge exhibits visible changes in the

spectra when measuring the brighter and darker regions (the displayed spectra have been normalized after linear background subtraction), which supports the structural analysis of the  $\mu$ -LEED and I(V)-LEEM data pointing to slight changes in the local environment of the Sm atoms. Although a comprehensive quantitative study through multiplet simulations [56] is beyond the scope of this work, it should be noted that previous reports [57] have shown that different surface orientations of single crystals lead to a similar variation of the absorption spectra. In particular, nonresonant inelastic hard x-ray scattering (NIXS) spectra across the  $\text{Sm } N_{4,5}$  edges of samarium compounds display a directional dependence, especially in the dipole transition region. In addition to the discussed differences in the absorption curves, there also exists a significant variation in the I(V)-LEEM curves extracted from the two regions marked in Fig. 7a, similar to those already shown in Fig. 6, confirming the existence of local variations of the Sm cations environment while retaining the  $\text{Sm}^{3+}$  oxidation state. The differences between  $\text{Sm } M_{4,5}$  and  $\text{Sm } N_{4,5}$  edges spectra could be related to the occupation (or mixing) degree of the 4f/5d states. For ceria, its I(V) curve is known to be strongly affected by a change in 4f occupation as it affects the nature of the unoccupied 5d states that largely determine the shape of the I(V) curve in this energy range [36]. Consequently, if samaria behaves similarly to ceria, then the different behavior of the XAS datasets presented in Fig. 7 could hint toward a stronger influence of the unoccupied 5d states on the  $\text{Sm } N_{4,5}$  absorption spectrum as compared to the one recorded at the  $\text{Sm } M_{4,5}$  edge.

#### 4. Conclusions

The growth and stability of samarium oxide on Ru(0001) grown by reactive physical vapor deposition were studied using high-resolution low-energy electron microscopy (LEEM), diffraction ( $\mu$ -LEED), and X-ray absorption spectroscopy carried out in photoemission electron microscopy mode (XAS-PEEM). Through a detailed LEEM and  $\mu$ LEED based structural analysis, our results show the formation of hexagonal  $\text{A-Sm}_2\text{O}_3$  islands during growth, in contrast with the usual stabilization of monoclinic and cubic phases at mild conditions for bulk samaria, i.e. powders and single crystals. The initial formation of the hexagonal phase can be explained by the strong influence of the substrate. These  $\text{Sm}_2\text{O}_3(0001)$  islands exhibit a hexagonal ( $1.38 \times 1.38$ ) LEED pattern with respect to the Ru(0001) substrate, which is consistent with an essentially unstrained bulk-like samaria structure. In addition, certain azimuthally rotated domains are identified, indicating that there are different configurations of how samaria can form a coincidence lattice with the underlying Ru surface. Furthermore, the formation of the exotic hexagonal phase at mild conditions was confirmed by comparing between experimental and theoretical (00)-beam I(V) curves from *ab initio* scattering theory for the cubic and hexagonal structures. Reciprocal space maps extracted from energy-dependent  $\mu$ -LEED patterns showed

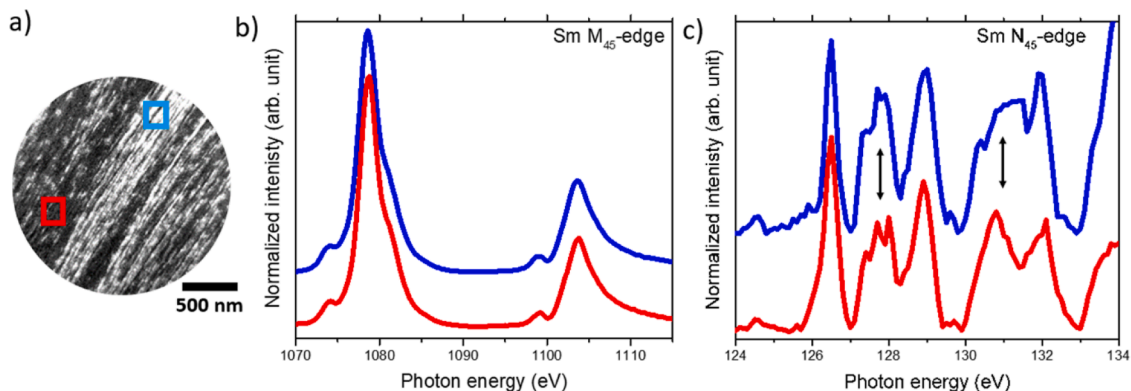


Fig. 7. a) LEEM image of the region where  $\text{Sm } M_{4,5}$  (b) and  $\text{Sm } N_{4,5}$  (c) XAS spectra were taken at 350 K. The red and blue squares in (a) indicate the local regions from where the XAS spectra have been extracted (displayed with the same color). For sake of clarity, the spectra have been shifted vertically.

the existence of (113) side facets of the hexagonal phase.

By keeping the sample at 350 K, we observe a gradual transition from the hexagonal to the more stable cubic phase, as confirmed by the I(V) curves. In particular, DF-LEEM analysis reveals a mixture of islands with C-Sm<sub>2</sub>O<sub>3</sub> and A-Sm<sub>2</sub>O<sub>3</sub> phases. Despite these local structural changes, samaria remains fully oxidized, as confirmed by local XAS data collected near the Sm M<sub>4,5</sub> edge, whereas the Sm N<sub>4,5</sub> spectra have been shown to be more sensitive to local variations in the Sm cations environment.

The unexpected initial growth in the A-Sm<sub>2</sub>O<sub>3</sub> hexagonal phase with distinct side facets and its gradual transition to a mixture with cubic C-Sm<sub>2</sub>O<sub>3</sub> highlights the complexity of the system and the critical role of the substrate in the stabilization of phases that for bulk samaria were previously shown to be stable only at very high pressures and temperatures. Besides, these results highlight the potential interactions that Sm could have with other catalytic compounds (e.g., the host material and substrate) and the influence of the preparation conditions.

### Declaration of Competing Interest

The authors declare that they have no known competing financial interests or personal relationships that could have appeared to influence the work reported in this paper.

### Data availability

Data will be made available on request.

### Acknowledgments

Measurements were carried out at the SMART endstation at the BESSY II electron storage ring operated by the Helmholtz-Zentrum Berlin für Materialien und Energie. We would also like to thank the Helmholtz-Center Berlin for Materials and Energy (HZB) for the allocation of beamtime 211–10186-ST. We gratefully acknowledge financial support from HZB. The SMART instrument was financially supported by the Federal German Ministry of Education and Research (BMBF) under the contract 05 KS4WWB/4, as well as by the Max-Planck Society. L.d.S. C. is grateful for the funding through the Deutsche Forschungsgemeinschaft (DFG, German Research Foundation) under Germany's Excellence Strategy-EXC 2008-390540038 (UniSysCat). M.J.P. was funded by German Federal Ministry of Education and Research (BMBF) under Grant No. 03EW0015B (CatLab). A.T. thanks the Alexander von Humboldt Foundation for the financial support. We acknowledge the support by the Spanish Ministry of Science, Innovation and Universities (Project No. PID2019–105488GB-I00). C. Morales acknowledges the Postdoc Network Brandenburg for a PNB grant. We thank Guido Beuckert for technical support.

### References

- G.V. Antoshin, K.M. Minachev, R.v. Dmitriev, Kinetics of isotope exchange in cerium dioxide-oxygen system, *Russ. J. Phys. Chem.* (1967) 1587.
- E. Ginting, S. Hu, J. Thome, Z. Yinghui, Z. Junfa, Z. Jing, Interaction of Mn with reducible CeO<sub>2</sub>(1 1 1) thin films, *Appl. Surf. Sci.* 283 (2013) 1–5.
- T. Skála, F. Sutara, K.C. Prince, V. Matolín, Cerium oxide stoichiometry alteration via Sn deposition: influence of temperature, *J. Electron. Spectros. Relat. Phenomena* 169 (2009) 20–25.
- G. Liu, J.A. Rodriguez, J. Hrbek, J. Dvorak, C.H.F. Peden, Electronic and chemical properties of Ce<sub>0.8</sub>Zr<sub>0.2</sub>O<sub>2</sub>(1 1 1) surfaces: photoemission, XANES, density-functional, and NO<sub>2</sub> adsorption studies, *J. Phys. Chem. B* 105 (2001) 7762–7770.
- Y. Wang, S. Hu, Q. Xu, H. Ju, J. Zhu, Sm on CeO<sub>2</sub>(111): a case for ceria modification via strong metal–ceria interaction, *Top. Catal.* 61 (2018) 1227–1236.
- S.D. Senanayake, P.J. Ramirez, I. Waluyo, S. Kundu, K. Mudiyansele, Z. Liu, Z. Liu, S. Axnanda, D.J. Stacchiola, J. Evans, J.A. Rodriguez, Hydrogenation of CO<sub>2</sub> to methanol on CeO<sub>x</sub>/Cu(111) and ZnO/Cu(111) catalysts: role of the metal-oxide interface and importance of Ce<sup>3+</sup> Sites, *J. Phys. Chem. C* 120 (2016) 1778–1784.
- J. Graciani, K. Mudiyansele, F. Xu, A.E. Baber, J. Evans, S.D. Senanayake, D. J. Stacchiola, P. Liu, J. Hrbek, J.F. Sanz, J.A. Rodriguez, Highly active copper-ceria and copper-ceria-titania catalysts for methanol synthesis from CO<sub>2</sub>, *Science* 345 (2014) 546–550.
- G. Niu, M.H. Zoellner, T. Schroeder, A. Schaefer, J.H. Jhang, V. Zielasek, M. Baumeier, H. Wilkens, J. Wollschlaeger, R. Olbrich, C. Lammers, M. Reichling, Controlling the physics and chemistry of binary and ternary praseodymium and cerium oxide systems, *Phys. Chem. Chem. Phys.* 17 (2015) 24513.
- M. Wuttig, X.D. Liu, Ultrathin metal films. Magnetic and structural properties, *Springer Tracts Mod. Phys.* (2004) 1–4.
- Y. Lei, et al., The role of samarium on Cu/Al<sub>2</sub>O<sub>3</sub> catalyst in the methanol steam reforming for hydrogen production, *Catal. Today* 307 (2018) 162–168.
- J. Zhu, Y. Ma, S. Zhuang, Exploring the role of samarium in the modification of rhodium catalysts through surface science approach, *Surf. Sci.* 603 (2009) 1802–1811.
- J.B. Wang, Y.L. Tai, W.P. Dow, T.J. Huang, Study of ceria-supported nickel catalyst and effect of yttria doping on carbon dioxide reforming of methane, *Appl. Catal. A Gen.* 218 (2001) 69–79.
- R.T. Baker, L.M. Gómez-Sainero, I.S. Metcalfe, Pretreatment-induced nanostructural evolution in CeO<sub>2</sub>-, Sm<sub>2</sub>O<sub>3</sub>-, and CeO<sub>2</sub>/Sm<sub>2</sub>O<sub>3</sub>-supported Pd catalysts for intermediate-temperature methanol fuel cells, *J. Phys. Chem. C* 113 (2009) 12465–12475.
- Y. Nakayama, H. Kondoh, T. Ohta, Coordination-dependent valence state of Sm adsorbed on Cu (100) and (110) studied by STM and XPS, *Surf. Sci.* 600 (2006) 2403–2410.
- J.H. Jhang, A. Schaefer, W. Cartas, S. Epuri, M. Bäumer, J.F. Weaver, Growth and Partial Reduction of Sm<sub>2</sub>O<sub>3</sub>(111) Thin Films on Pt(111): evidence for the Formation of SmO(100), *J. Phys. Chem. C* 3 (2013).
- M. Kuchowicz, J. Kolaczkiwicz, Valence changes of Sm atoms adsorbed on Mo (2 1 1) surface, *Surf. Sci.* 602 (2008) 3721–3727.
- M. Kuchowicz, Coadsorption of samarium with oxygen on the molybdenum (2 1 1) surface, *Appl. Surf. Sci.* 256 (2010) 4818–4821.
- X. Qian, S. Hu, D. Cheng, X. Feng, Y. Han, J. Zhu, Growth and electronic structure of Sm on thin Al<sub>2</sub>O<sub>3</sub>/Ni<sub>3</sub>Al(111) films, *J. Chem. Phys.* 136 (2012).
- S. Jiang, J. Liu, C. Lin, X. Li, Y. Li, High-pressure x-ray diffraction and Raman spectroscopy of phase transitions in Sm<sub>2</sub>O<sub>3</sub>, *J. Appl. Phys.* 113 (2013), 113502.
- M. Zinkevich, Thermodynamics of rare earth sesquioxides, *Prog. Mater. Sci.* 52 (2007) 597–647.
- S. Tresvyatkii, L.M. Lopato, A.W. Schwetschenko, Untersuchung des einflusses hochschmelzender oxide der elemente II. Gruppe des periodischen systems. Auf polymorphe hochtemperatur-umwandlungen von oxiden der seltenerdelemente, *Colloq. Intern. Cent. Natl. Rech. Sci. Paris* 205 (1971) 247–253.
- A.v. Shevchenko, L.M. Lopato, DTA method application to the highest refractory oxide systems investigation, *Thermochim. Acta* 93 (1985) 537–540.
- B. Wu, M. Zinkevich, F. Aldinger, D. Wen, L. Chen, Ab initio study on structure and phase transition of A- and B-type rare-earth sesquioxides Ln<sub>2</sub>O<sub>3</sub> (Ln=La–Lu, Y, and Sc) based on density function theory, *J. Solid State Chem.* 180 (2007) 3280–3287.
- Q. Guo, Y. Zhao, C. Jiang, W.L. Mao, Z. Wang, Phase transformation in Sm<sub>2</sub>O<sub>3</sub> at high pressure: in situ synchrotron X-ray diffraction study and ab initio DFT calculation, *Solid State Commun* 145 (2008) 250–254.
- J.-F. Martel, S. Jandl, A.M. Lejus, B. Viana, D. J. Vivien, Optical crystal field study of Sm<sub>2</sub>O<sub>3</sub> (C- and B-type), *J. Alloys Compd.* 275–277 (1998) 353–355.
- A. AmaliRoselin, N. Anandhan, G. Ravi, M. Mummoorthi, T. Marimuthu, Growth and characterization of Sm<sub>2</sub>O<sub>3</sub> thin films by spin coating technique, *Journal of ChemTech Research* (2014) 5315–5320.
- T.A.M. Onik, H.F. Hawari, M.F.M. Sabri, Y.H. Wong, Growth mechanisms and characteristics of Sm<sub>2</sub>O<sub>3</sub> based on Ge semiconductor through oxidation and nitridation, *Appl. Surf. Sci.* 544 (2021), 148949.
- J. Höcker, T. Duchon, J. Falta, S.D. Senanayake, J.I. Flége, Controlling heteroepitaxy by oxygen chemical potential: exclusive growth of (100) oriented ceria nanostructures on Cu(111), *J. Phys. Chem. C* (2016) 4895–4901.
- J.I. Flége, J. Höcker, B. Kaemena, T.O. Menteş, A. Sala, A. Locatelli, S. Gangopadhyay, J.T. Sadowski, S.D. Senanayake, J. Falta, Growth and characterization of epitaxially stabilized ceria(001) nanostructures on Ru(0001), *Nanoscale* 8 (2016) 10849–10856.
- G. Vilé, S. Colussi, F. Krumeich, A. Trovarelli, J. Pérez-Ramírez, Opposite face sensitivity of CeO<sub>2</sub> in hydrogenation and oxidation catalysis, *Ang. Chem. Int. Ed.* 53 (2014) 12069–12072.
- D.R. Mullins, P.M. Albrecht, F. Calaza, Variations in reactivity on different crystallographic orientations of cerium oxide, *Top. Catal.* 56 (2013) 1345–1362.
- J.I. Flége, E.E. Krasovskii, Intensity-voltage low-energy electron microscopy for functional materials characterization, *Physica Status Solidi* 8 (2014) 463–477.
- T. Schmidt, et al., Double aberration correction in a low-energy electron microscope, *Ultramicroscopy* 110 (2010) 1358–1361.
- J.L.F. da Silva, Stability of the Ce<sub>2</sub>O<sub>3</sub> phases: a DFT+U investigation, *Phys. Rev. B Condens. Matter Mater. Phys.* 76 (2007), 193108.
- E.E. Krasovskii, Augmented-plane-wave approach to scattering of Bloch electrons by an interface, *Phys. Rev. B* 70 (2004) 245–322.
- J.I. Flége, B. Kaemena, A. Meyer, J. Falta, Origin of chemical contrast in low-energy electron reflectivity of correlated multivalent oxides: the case of ceria, *Phys. Rev. B Condens. Matter Mater. Phys.* 88 (2013).
- J.I. Flége, J.O. Krispeneit, J. Höcker, M. Hoppe, Y. Niu, A. Zakharov, A. Schaefer, J. Falta, E.E. Krasovskii, Nanoscale analysis of the oxidation state and surface termination of praseodymium oxide ultrathin films on ruthenium(0001), *Ultramicroscopy* 183 (2017) 1339–1351.
- J.I. Flége, B. Kaemena, S.D. Senanayake, J. Höcker, J.T. Sadowski, J. Falta, Growth mode and oxidation state analysis of individual cerium oxide islands on Ru(0001), *Ultramicroscopy* 130 (2013) 87–93.

- [39] P. Luches, G. Gasperi, M. Sauerbrey, S. Valeri, J. Falta, J.I. Flege, Dynamics of the interaction between ceria and platinum during redox processes, *Front. Chem.* 7 (2019).
- [40] J. Höcker, T.O. Mentès, A. Sala, A. Locatelli, T. Schmidt, J. Falta, S.D. Senanayake, J.I. Flege, Unraveling the dynamic nanoscale reducibility (Ce 4+→Ce 3+) of CeOx – Ru in hydrogen activation, *Adv. Mat. Interfaces* (2015) 1–6.
- [41] T. Schmidt, T. Clausen, J.I. Flege, S. Gangopadhyay, A. Locatelli, T.O. Mentès, F. Z. Guo, S. Heun, J. Falta, Adsorbate induced self-ordering of germanium nanoislands on Si(113), *New J. Phys.* 9 (2007) 392.
- [42] F.J. Meyer zu Heringdorf, M. Horn-von Hoegen, Reciprocal space mapping by spot profile analyzing low energy electron diffraction, *Rev. Sci. Instr.* 76 (2005), 085102.
- [43] M. Horn-von Hoegen, Growth of semiconductor layers studied by spot profile analyzing low energy electron diffraction - Part I, *Zeitschrift für Kristallographie - New Crystal Structures* 214 (1999) 591–629.
- [44] I. Krug, N. Barrett, A. Petraru, A. Locatelli, T.O. Mentès, M.A. Niño, et al., Extrinsic screening of ferroelectric domains in Pb(Zr0.48Ti0.52)O3, *Appl. Phys. Lett.* 97 (2010) 22.
- [45] J.L. Wang, B. Vilquin, N. Barrett, Screening of ferroelectric domains on BaTiO3 (001) surface by ultraviolet photo-induced charge and dissociative water adsorption, *Appl. Phys. Lett.* 101 (2012) 9.
- [46] Artur; Boettcher, H. Niehus, Oxygen adsorbed on oxidized Ru (0001), *Phys. Rev. B* 60 (1999) 396–404.
- [47] A.-B. Yang, A photoemission study of samarium on silicon. *Retrospective Theses and Dissertations* 9254, 1989.
- [48] S.A. Surma, J. Brona, A. Ciszewski, Electron work functions of (h kl)-surfaces of W, Re, and Cu crystals, *Mater. Sci.-Pol.* 36 (2018) 225–234.
- [49] K.F. Wojciechowski, Application of Brodie's concept of the work function to simple metals, *Europhys. Lett.* 38 (1997) 135–140.
- [50] J. Wang, S.Q. Wang, Surface energy and work function of fcc and bcc crystals: density functional study, *Surf Sci* 630 (2014) 216–224.
- [51] G. Bunker, Introduction to XAFS: a Practical Guide to X-ray Absorption Fine Structure Spectroscopy, *Introductions to XAFS* (2010).
- [52] A. Osamu, W. Takeshi, F. Yoshihiko, T. Kenjiro, Sm M4,5 Spectra of Metallic Samarium and Samarium Hexaboride, *J. Phys. Soc. Japan* 51 (2013) 483–489.
- [53] J. Sahu, S. Kumar, P.A. Alvi, D.M. Phase, M. Gupta, S. Dalela, Study of structural, optical and electronic structure properties of Sm2O3-ZnO nanomaterials, *AIP Conf. Proc* 2265 (2020), 030130.
- [54] A. Sharma, M. Varshney, H.J. Shin, K.H. Chae, S.O. Won, Investigation on cation distribution and luminescence in spinel phase  $\gamma$ -Ga3–8O4: Sm nanostructures using X-ray absorption spectroscopy, *RSC Adv.* 7 (2017) 52543–52554.
- [55] G. Kaindl, G. Kalkowski, W.D. Brewer, B. Perscheid, F. Holtzberg, M-edge x-ray absorption spectroscopy of 4f instabilities in rare-earth systems (invited), *J. Appl. Phys.* 55 (1984) 1910–1915.
- [56] P. Miedema, F. De Groot, The iron L edges: fe 2p X-ray absorption and electron energy loss spectroscopy, *J. Electron Spectrosc. Relat. Phenom.* 187 (2013) 34–48.
- [57] M. Sundermann, H. Yavaş, K. Chen, D.J. Kim, Z. Fisk, M.W. Kasinathan, Haverkort, P. Thalmeier, A. Severing, L.H. Tjeng, 4f crystal field ground state of the strongly correlated topological insulator SmB6, *Phys. Rev. Lett.* 120 (2018).